Nano Research
2021, 14(11): 4107–4115

ISSN 1998-0124 CN 11-5974/O4
https://doi.org/10.1007/s12274-021-3350-y

Multiband emission from single β-$NaYF_4$(Yb,Er) nanoparticles at high excitation power densities and comparison to ensemble studies

Florian Frenzel[1,4], Christian Würth[1], Oleksii Dukhno[2], Frédéric Przybilla[2], Lisa M. Wiesholler[3], Verena Muhr[3], Thomas Hirsch[3], Yves Mély[2], and Ute Resch-Genger[1] (✉)

[1] *Federal Institute for Materials Research and Testing (BAM), Division 1.2 Biophotonics, Richard-Willstaetter -Str. 11, 12489 Berlin, Germany*
[2] *Laboratory of Biomaging and Pathologies, UMR 7021 CNRS, University of Strasbourg, 67000 Strasbourg, France*
[3] *Institute of Analytical Chemistry, Chemo- and Biosensors, University of Regensburg, 93040 Regensburg, Germany*
[4] *Institut für Physik and IRIS Adlershof, Humboldt-Universität zu Berlin, Newtonstraße 15, 12489 Berlin, Germany*

Received: 17 October 2020 / **Revised:** 17 January 2021 / **Accepted:** 20 January 2021

ABSTRACT

Ensemble and single particle studies of the excitation power density (P)-dependent upconversion luminescence (UCL) of core and core–shell β-$NaYF_4$:Yb,Er upconversion nanoparticles (UCNPs) doped with 20% Yb^{3+} and 1% or 3% Er^{3+} performed over a P regime of 6 orders of magnitude reveal an increasing contribution of the emission from high energy Er^{3+} levels at $P > 1$ kW/cm^2. This changes the overall emission color from initially green over yellow to white. While initially the green and with increasing P the red emission dominate in ensemble measurements at $P < 1$ kW/cm^2, the increasing population of higher Er^{3+} energy levels by multiphotonic processes at higher P in single particle studies results in a multitude of emission bands in the ultraviolet/visible/near infrared (UV/vis/NIR) accompanied by a decreased contribution of the red luminescence. Based upon a thorough analysis of the P-dependence of UCL, the emission bands activated at high P were grouped and assigned to 2–3, 3–4, and 4 photonic processes involving energy transfer (ET), excited-state absorption (ESA), cross-relaxation (CR), back energy transfer (BET), and non-radiative relaxation processes (nRP). This underlines the P-tunability of UCNP brightness and color and highlights the potential of P-dependent measurements for mechanistic studies required to manifest the population pathways of the different Er^{3+} levels.

KEYWORDS

upconversion luminescence, single nanoparticle study, high power excitation, emission color, luminescence decay kinetics

1 Introduction

Lanthanide-based upconversion nanoparticles (UCNPs) with their photoluminescence (PL) in the ultraviolet (UV), visible (vis), and near infrared (NIR) following the absorption of two or more low energy photons have been increasingly studied in the last years [1–6]. These spectrally shifting inorganic nanocrystals with their excitation power density (P)-dependent luminescence typically consist of a host matrix such as $NaYF_4$, doped with light-absorbing sensitizer Yb^{3+} ions and the emissive activator ions Tm^{3+}, Er^{3+} or Ho^{3+}. For the observation of upconversion luminescence (UCL) from the activator ions in the UV/vis/NIR, e.g., in optical assays and applications in sensing [7, 8], optogenetics [9–11], anticounterfeiting, barcoding [12], photovoltaics [4, 13] and super-resolution microscopy [14], these Yb-sensitized UCNPs are excited at 980 nm. As revealed by many photophysical studies of UCNPs of different size [15, 16], doping ion concentration, and particle architecture in apolar solvents and aqueous environments [17, 18], the intensity and relative spectral distribution of UCL are controlled by the interplay of energy transfer (ET) processes between the lanthanide doping ions involved in the (de)population of the radiative energy levels of the activator ions. These ET processes depend on the distances between the different lanthanide ions and hence on host crystal phase and symmetry, as well as on the concentration and spatial arrangement of the doping ions. In addition, the emission behavior of UCNPs is also determined by quenching processes related to surface defects and the presence of molecules or ions containing high energy vibrators such as –OH groups. Therefore, UCL intensity can be enhanced by a surface passivation shell protecting the emissive lanthanide ions from such quenchers that must have a certain thickness and should be tight [19].

Due to their excellent photostability, UCNPs have gained interest as reporter for fluorescence microscopy using high P in the range of kW/cm^2 to MW/cm^2. Emerging applications include single particle (SP) tracking and super-resolution microscopy [14, 20]. This initiated an increasing number of spectroscopic studies of these nanomaterials on the SP level [21–23], assessing UCL features with the overall goal to identify optimum particle architectures for these high P regimes. However, SP studies always raise the question of the particle-to-particle comparability of the luminescence properties, which can be affected by particle preparation and shelling procedures.

With the aim to correlate UCL ensemble spectroscopic measurements and high P microscopic studies and gain a deeper mechanistic insight into the (de)population processes at $P > 1{,}000$ W/cm^2, we assessed the optical properties of a set of 28 nm-sized core and core–shell UCNPs doped with 20% Yb^{3+} and 1% or 3% Er^{3+} at low, medium as well as high P.

Address correspondence to Ute.Resch@bam.de

To enable ensemble and SP spectroscopic measurements in an overlapping *P* regime, we built up a very sensitive SP setup equipped with a CCD detector applicable for spectroscopic studies of single UCNPs at *P* of 1 kW/cm^2 up to 2.6 MW/cm^2. The results of our study demonstrate the previously shown potential of *P* to tune UCL color and intensity [24] and more importantly show the influence of (de)populating higher Er^{3+} energy levels on UCL spectral distribution. In SP studies the enhanced population of higher Er^{3+} energy levels by multiphotonic processes at higher *P* leads to a multitude of emission bands in the UV/vis/NIR accompanied by a decrease in the contribution of the red luminescence. Moreover, based upon an in-depth analysis of the *P*-dependence of UCL, we derived a classification of the different high *P*-activated emission bands and their assignment to 2–3, 3–4, and 4 photonic processes.

2 Results and discussion

2.1 Ensemble spectroscopic studies in cyclohexane

For our mechanistic studies we chose a set of four core only (co) and core–shell (cs) UCNPs (5 nm-thick $NaYF_4$ shell) (Fig. 1(a)) of similar size doped with 1% and 3% Er^{3+}. Such UCNPs are used by many research groups. *P*-dependent spectroscopic studies of our samples dispersed in cyclohexane revealed the small influence of the Er^{3+} dopant concentration in this concentration range and the expected effect of the surface protecting shell on the relative spectral distribution and efficiency of UCL. The spectrally corrected normalized emission spectra weighted by the absorption factor, recorded at $P = 200$ W/cm^2 are shown in Fig. 1(b). These spectra reveal the typical UCL enhancement introduced by an inert $NaYF_4$ shell [25], thereby enhancing the green and red Er^{3+} emission by factors of 5 and 6. In addition, the slight increase in Er^{3+} doping concentration from 1% to 3% further enhances the intensities of the green and red emission bands of the cs NPs by 30% (Fig. 1(b)). As shown in Fig. 1(c), the *P*-dependences of the green (510–570 nm) and red (630–685 nm) emission that together account for about 80% of the total UCL in ensemble measurements, display opposite trends. While the green emission is favored at low *P*, the red one dominates at higher *P*. This behavior is typical for β-$NaYF_4$:Yb^{3+}, Er^{3+} with sizes larger than 23 nm [15]. As revealed in Fig. 1(c) by the crossing points of the green (G) and red (R) intensities highlighting an equal ratio of both emission bands (G/R = 1), for the core particles the green emission dominates for $P < 50$ W/cm^2, whereas for the cs systems the red emission dominates already at lower *P* (~ 10 W/cm^2). For the cs systems the relative spectral distribution of the luminescence reaches a constant value at $P > 300$ W/cm^2 indicating equilibrated population rates of the involved Er^{3+} energy levels. This is in good agreement with previous studies [15, 16].

2.2 Single particle studies

2.2.1 *Correlated atomic force microscopy (AFM)-PL single UCNP measurements*

For the correlated AFM-PL measurements to indicate the presence of single UCNPs and for the PL studies of single UCNPs we used a custom designed setup consisting of an inverse microscope combined with an AFM (Section S4 in the Electronic Supplementary Material (ESM)) that provides a sub-nanometer resolution in height and visualizes both bright (emissive) and dark (non-emissive) NPs. In Fig. 2(a), the bright spots obtained with widefield imaging (WI) under combined white-light and 980 nm laser illumination represent emissive cs UCNPs. CdSe nanowires (excited at 405 nm) serve as alignment markers to correlate diffraction limited PL imaging and AFM (Fig. 2(b)). Correlating diffraction limited PL imaging (Fig. 2(c)) and AFM in an AFM-PL overlay (Fig. 2(d)) allows

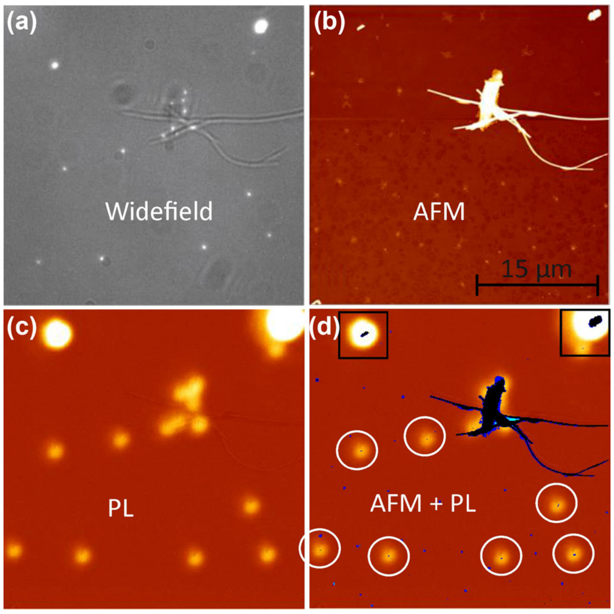

Figure 2 Combined AFM and PL scans of core–shell UCNPs. (a) Widefield image obtained with monochrome camera under combined white-light and 980 nm laser illumination of UCNP sample and nanowires dried on a glass substrate. (b) AFM scan of the same region. (c) Diffraction limited PL scan under 980 nm excitation measured with APD of the confocal microscope setup. (d) Overlay of the AFM (in blue) and confocal PL image. Single UCNPs are indicated by white circles and aggregates by black squares.

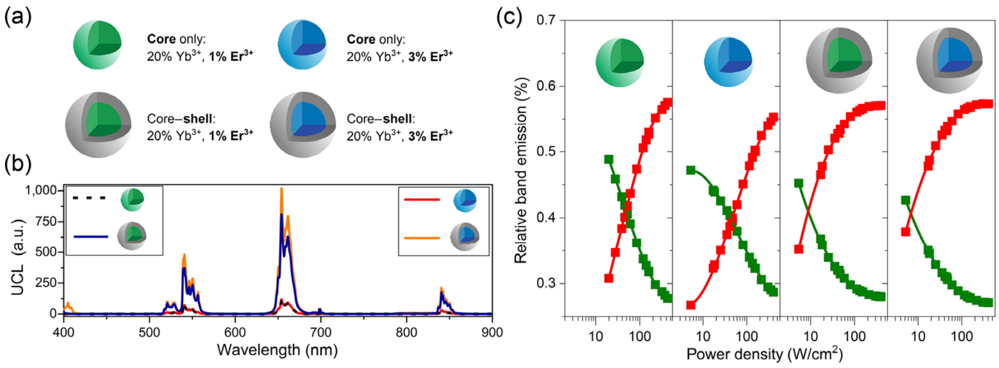

Figure 1 Overview of the ensemble studies. (a) Set of hexagonal β-$NaYF_4$:x% Er^{3+}, 20% Yb^{3+} core/core–shell UCNPs (x = 1, 3) used in this study. (b) Absorption-normalized UCL spectra of the four samples dispersed in cyclohexane measured in ensemble conditions at $P = 200$ W/cm^2. (c) *P*-dependent ensemble measurements of the relative spectral contribution of the green ($^2H_{11/2}$ and $^4S_{3/2}$) and red ($^4F_{9/2}$) UCL bands of Er^{3+} of the four samples dispersed in cyclohexane in the *P* range of 5 up to 400 W/cm^2.

to identify single UCNPs (white circles) and aggregates (black squares). In Figs. S5(a) and S5(b) in the ESM, close-ups of a single core and a core–shell NP are presented proofing the SP nature. Both types of UCNPs are clearly distinguishable in shape and height from UCNP aggregates that can be formed during sample preparation (Fig. S5(c) in the ESM).

2.2.2 *Particle-to-particle variations in PL features*

Widefield imaging was used to obtain brightness distribution histograms of the green and red Er^{3+} emission of our UCNPs with the setup shown in Fig. S3(a) in the ESM and the methodology described in detail in our previous work [26]. A Gaussian fit of these distributions provides a measure for particle-to-particle differences in terms of brightness. Figures 3(a)–3(d) summarize the UCL histograms of the four UCNP systems with their Gaussian-like brightness distributions (including standard deviations (σ_λ)) for the green and red Er^{3+} emission obtained at $P = 8$ kW/cm². The very small number of outliers confirms that the signals derived from the least bright particle population really originate from single UCNPs. Both co UCNPs show a wider intensity distribution for the red (r) than for the green (g) emission (for 1% Er^{3+}: $\sigma_r^{co} \approx 1.4\sigma_g^{co}$ and for 3% Er^{3+}: $\sigma_r^{co} \approx 1.2\sigma_g^{co}$). This could be caused by local differences in P in combination with the higher photonic order of the red emission band. Increasing the Er^{3+} doping concentration from 1% to 3% enhances the green and red emission of the co particles by factors of 2.3 and 1.8 (Figs. 3(a) and 3(c)). Shelling of the cores increases the green and red UCL of 1% Er^{3+}-doped UCNPs by factors of 3.5 and 2.3, respectively, without affecting the respective intensity distributions (Figs. 3(a) and 3(b)). The brightest UCNPs are cs UCNPs doped with 3% Er^{3+} (Figs. 3(c) and 3(d), and Fig. S3(b) in the ESM).

2.3 Ensemble vs. single NP studies

Studies of single UCNPs allow to explore the nonlinear UCL properties of UCNPs at very high P (> MW/cm²). To assess the UCL features at broadly varying P and to enable a correlation of ensemble measurements performed in the 5 to 400 W/cm² P range and SP studies, the latter were done at P as low as about 1 kW/cm² up to 2.6 MW/cm². As will be shown in a forthcoming section on luminescence decay kinetics, at high P, the influence of UCNP environment seems to be negligible.

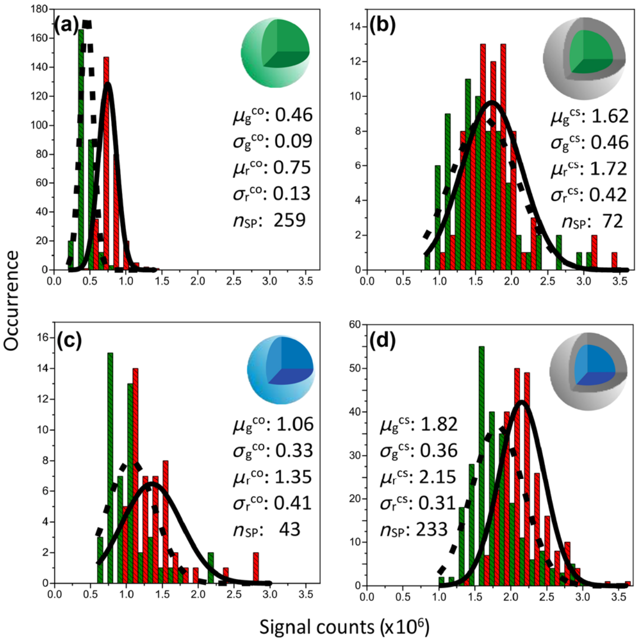

Figure 3 Brightness distribution histograms for the green and red emission bands. (a)–(d) The black dotted and solid lines are the Gaussian fits of the brightness distributions of the green (g) and red (r) emission bands with mean value μ and standard deviation σ of the core-only (co) and core–shell (cs) systems. The value n_{SP} is the number of SPs used for the measurements.

2.3.1 *P-dependent spectra of single UCNPs*

The UCL spectra of the four UCNP systems in the wavelength range of 390 to 810 nm recorded with P of 1 kW/cm² up to 2.6 MW/cm² are shown in Figs. S6(a)–S6(d) in the ESM. An averaged PL spectrum derived from five core–shell UCNPs doped with 3% Er^{3+} is shown in Fig. 4(a). Besides the typical Er^{3+} peaks at 410, 521, 541, 654, and 840 nm known from ensemble studies (Fig. 1(b)), this figure reveals a large number of new sharp emission bands located at 400, 410, 427, 440, 454, 468, 481, 495, 503, 506, 556, 575, 585, 616, 639, 699, 765 and 801 nm, which appear with increasing P. Due to the high spectral resolution of 0.43 nm of the SP setup, even sharp emission bands at 405, 527, 610, 662, 712, 724, and 750 nm could be identified. The appearance of all new bands leads to a change in the overall emission color of the UCNPs from green to yellow to white with increasing P. This color change is highlighted in the CIE (Commission Internationale de l'Éclairage) diagram in Fig. 4(a).

The influence of the protective shell and the Er^{3+} doping concentration on the P-dependent UCL features and the total emission color can be derived from a comparison of the UCL spectra and the CIE diagram provided in Figs. S6(a)–S6(d) and S6(j) in the ESM. These figures reveal overall similar trends for all UCL emission bands but slightly different dependencies for the different Er doping concentrations. The latter are ascribed to the changed Er^{3+}–Er^{3+} distances resulting in slightly different ET rates of the (de)population processes of the radiative Er^{3+} energy levels.

At P below 10 kW/cm², the integrated UCL (Fig. S6(e) in the ESM) obtained from the cs UCNPs clearly exceeds those of the co UCNPs. With increasing P (> 20 kW/cm²), the influence of surface quenching and hence passivation by the protective shell decreases. At higher P the population rates considerably overweight the quenching rates.

To investigate the high energy Er^{3+} levels accounting for the newly observed emission bands, we subsequently focused on the main peaks, which can be clearly distinguished from each other without the need of a spectral deconvolution to separate signal contributions from neighboring, spectrally overlapping bands. These peaks were then divided into three groups based upon the P-dependence of their UCL intensities as shown in Figs. 4(b)–4(d). A Dieke diagram (Fig. 4(e)) relying on Judd-Ofelt analyses [27–31] was used for clarifying the complex population processes of the Yb^{3+}–Er^{3+} system involving ET, excited-state absorption (ESA) of Er^{3+}, cross-relaxation (CR), Er^{3+}–Yb^{3+} back energy transfer (BET), and non-radiative relaxation processes (nRP).

2.3.2 *Grouping of P-dependent emission bands and processes*

The first group of emission bands—peaking at 410 nm ($^2H_{9/2} \rightarrow {}^4I_{15/2}$), 521 nm ($^2H_{11/2} \rightarrow {}^4I_{15/2}$), 541 nm ($^4S_{3/2} \rightarrow {}^4I_{15/2}$), 556 nm ($^2H_{9/2} \rightarrow {}^4I_{13/2}$), 654 nm ($^4F_{9/2} \rightarrow {}^4I_{15/2}$), and 699 nm ($^2H_{9/2} \rightarrow {}^4I_{11/2}$)—is already present at low P of 1 kW/cm² and shows maximum intensities at about 600 kW/cm² (Fig. 4(b)). The energy levels responsible for these emission bands are populated by 2–3 photonic processes involving a first ET from Yb^{3+} ($^2F_{5/2}$) → Er^{3+} ($^4I_{11/2}$). The $^4F_{7/2}$ level can be populated from $^4I_{11/2}$ (green bars, 1+2) via a 2nd Yb → Er ET accounting for the emission bands at 521 nm and at 541 nm after nRP

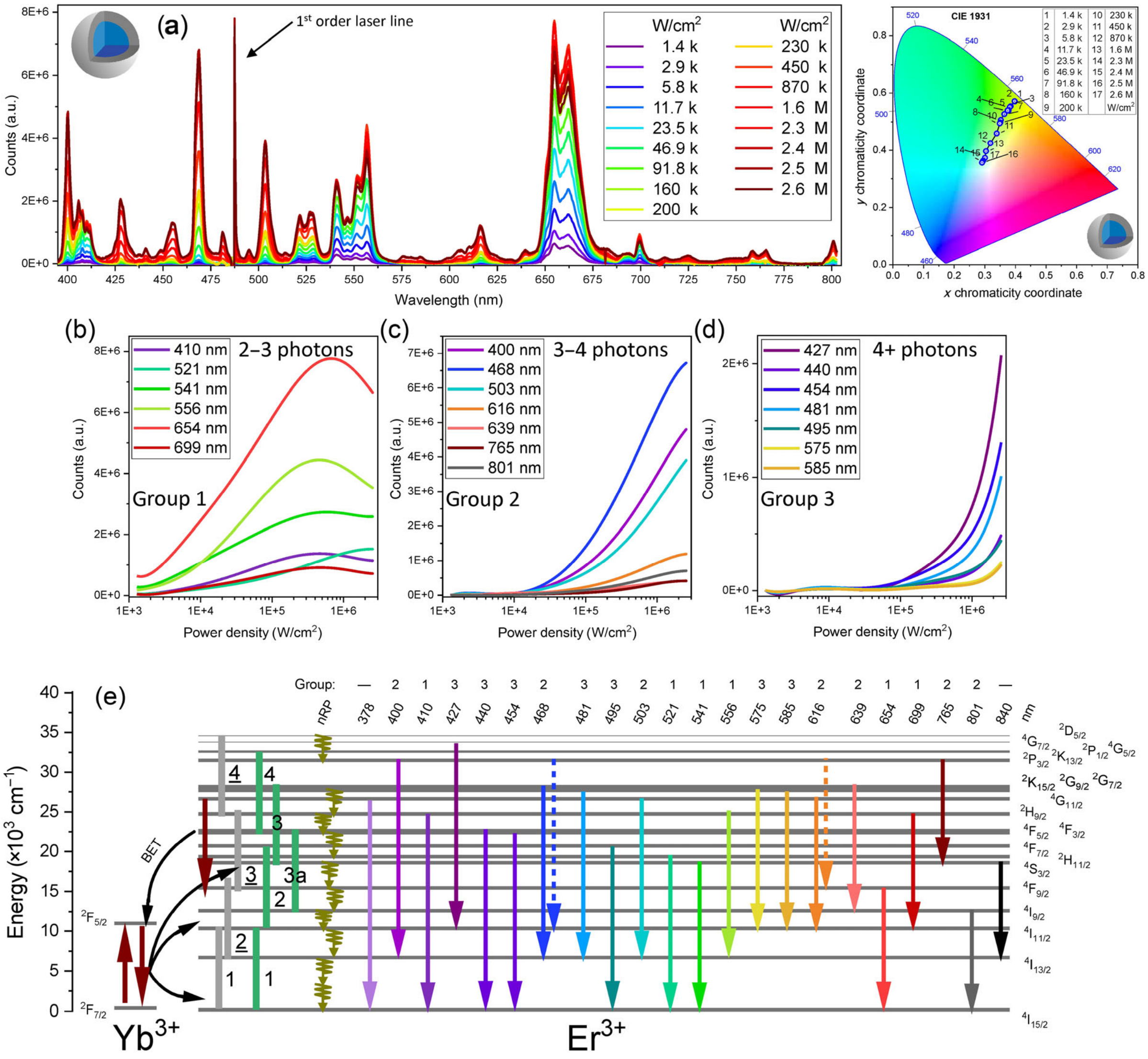

Figure 4 *P*-dependent UCL spectra of single core–shell UCNPs doped with 3% Er^{3+}. (a) *P*-dependent UCL spectra of core–shell UCNPs doped with 3% Er^{3+} obtained in the 390 to 810 nm wavelength region for *P* varying from kW to MW/cm². The CIE diagram shows the change in total emission color from green to yellow to white with increasing *P*. (b)–(d) *P*-dependence of selected strong emission bands classified into three groups with low, medium, and high *P* activated emission, corresponding to 2–3, 3–4 and 4 photonic processes. (e) Energy scheme of the Yb^{3+}–Er^{3+} system summarizing the processes yielding UCL and describing the origin of the most prominent emission bands in the wavelength region of 370 to 850 nm under 980 nm excitation.

from $^4F_{7/2}$ to $^2H_{11/2}$/$^4S_{3/2}$. These two green Er^{3+} emission bands reveal a slightly different *P* dependence. The 521 nm emission follows the *P*-dependent trend of the 541 nm emission, but with a shift to higher *P*. This is attributed to the thermal Boltzmann coupling between the $^4S_{3/2}$ and the $^2H_{11/2}$ level and an enhanced population from the lower to the higher energy level with increasing *P* [32–34]. In this medium *P* range, the red band ($^4F_{9/2}$) is expected to be populated via the well-known BET process from the Er^{3+} ^4G/^2K manifolds to Yb^{3+} ($^2F_{7/2} \rightarrow {}^2F_{5/2}$) [35]. This makes the population of $^4F_{9/2}$ a three photonic process (green bars, 1-3 + BET). Also, the 410 nm ($^2H_{9/2} \rightarrow {}^4I_{15/2}$), 556 nm ($^2H_{9/2} \rightarrow {}^4I_{13/2}$), and 699 nm ($^2H_{9/2} \rightarrow {}^4I_{11/2}$) emission bands originate from three photonic processes. Here, the $^2H_{9/2}$ level is either populated via nRP from the ^4G/^2K manifolds ($^2G_{7/2}$, $^2G_{9/2}$, $^2K_{15/2}$, $^4G_{11/2}$) or excited directly via a 3rd $Yb^{3+} \rightarrow Er^{3+}$ ET from $^4F_{9/2}$, (grey bar, 3) [24, 36]. The observed constant increase of the 654 nm emission below *P* of 600 kW/cm² is related to an increasingly occurring Er^{3+}–Yb^{3+} BET boosting Yb^{3+} excitation [35, 37]. The respective bands, involving two and three photonic processes, follow the same trend i.e., their intensities increase up to *P* of about 600 kW/cm² and then decrease again.

The emission bands of groups 2 and 3 appearing at comparably high *P* are favored by the already high population of the Er^{3+} energy levels. Here, enhanced contributions of ESA and a reduced Er^{3+}–Yb^{3+} BET due to the already high number of excited Yb^{3+} ions seem to play a significant role.

The second group of emission bands—peaking at 400 nm ($^2P_{3/2} \rightarrow {}^4I_{13/2}$), 468 nm ($^2G_{7/2} \rightarrow {}^4I_{13/2}$) & ($^2P_{3/2} \rightarrow {}^4I_{11/2}$), 503 nm ($^4G_{11/2} \rightarrow {}^4I_{13/2}$), 616 nm ($^4G_{11/2} \rightarrow {}^4I_{11/2}$) & ($^2P_{3/2} \rightarrow {}^4F_{9/2}$), 639 nm ($^2G_{7/2} \rightarrow {}^4I_{9/2}$), 765 nm ($^2P_{3/2} \rightarrow {}^4S_{3/2}$), and 801 nm ($^4I_{9/2} \rightarrow {}^4I_{15/2}$)—appear at *P* exceeding 10 kW/cm² and start to saturate for *P* exceeding 600 kW/cm².

Population of the emissive Er^{3+} energy levels $^4G_{11/2}$, $^2G_{7/2}$, and $^2P_{3/2}$ requires the absorption of at least 3 to 4 photons (Fig. 4(c)). ESA and ET lead to excitation of the energy level $^2G_{7/2}$ (leading to emission bands at 468 and 639 nm) by depopulation of the $^4S_{3/2}$ level (green bar, 3). This accounts for the decrease of the 541 nm emission at higher *P*. The energy level responsible for the 503 and 616 nm luminescence is fed via nRP from the energetically higher lying $^2K_{15/2}$ energy level. For the emission bands at 468 and 616 nm, also a contribution of radiative transitions from the high energy $^2P_{3/2}$ level is feasible (dashed arrows in Fig. 4(e)) [29]. To populate the $^2P_{3/2}$ level (responsible for the 400 nm emission) a minimum number of 4 photons must be absorbed. This can occur by ET and ESA from the $^4F_{5/2}/{}^4F_{3/2} \rightarrow {}^2K_{13/2}$ (green bar, 4) [29] or by ESA from the $^2H_{9/2} \rightarrow {}^2D_{5/2}$ (grey bar, $\underline{4}$) level. The latter acts as depopulation pathway of the $^2H_{9/2}$ energy level and could account for the drop of the intensities of the 410, 556, and 699 nm emission bands observed for P higher than 600 kW/cm^2 (Fig. 4(b)). The increase of the 801 nm emission from the comparably low lying $^4I_{9/2}$ energy level may be caused by enhanced Er^{3+}–Er^{3+} CR (donor: $^2H_{11/2}/{}^4S_{3/2} \rightarrow {}^4I_{9/2}$ and acceptor: $^4I_{15/2} \rightarrow {}^4I_{13/2}$, [38]), nRP from the energetically higher lying $^4F_{9/2}$ energy level or by the initially excited 639 nm luminescence originating from the $^2G_{7/2} \rightarrow {}^4I_{9/2}$ transition.

At $P > 100$ kW/cm^2 a third group of emission bands appears at 427 nm ($^4G_{7/2} \rightarrow {}^4I_{11/2}$), 440 nm ($^4F_{3/2} \rightarrow {}^4I_{15/2}$), 454 nm ($^4F_{5/2} \rightarrow {}^4I_{15/2}$), 481 nm ($^2K_{15/2} \rightarrow {}^4I_{13/2}$), 495 nm ($^4F_{7/2} \rightarrow {}^4I_{15/2}$), 575 nm ($^2G_{9/2} \rightarrow {}^4I_{11/2}$), and 585 nm ($^2K_{15/2} \rightarrow {}^4I_{11/2}$) as shown in Fig. 4(d). The explanation of the underlying processes at this high P is rather difficult as the population density of the Er^{3+} doping ions is already high and Er^{3+}–Er^{3+}, Er^{3+}–Yb^{3+} ET and ESA processes could be involved.

The 481, 575, and 585 nm emission bands may arise from multi-phonon relaxations (mpR) from the $^2G_{7/2}$ to the $^2G_{9/2}$ and $^2K_{15/2}$ energy levels following a 3-photonic absorption process including Er^{3+}–Er^{3+}, Er^{3+}–Yb^{3+} ET and ESA processes (green bars, 1–3). The 481 nm emission overlaps with the first order laser line and cannot be reliably analyzed (Fig. 4(a)). The increasing contributions of the 440, 454, and 495 nm emission bands at high P originating from the relatively low energy ^4F levels ($^4F_{3/2}$, $^4F_{5/2}$, and $^4F_{7/2}$) may be ascribed to an additional ESA (green bar, 3a) helping to cover the energy gap between $^4I_{9/2}$ to $^4F_{3/2}$ or Er^{3+}–Er^{3+} ET bridging the respective energy gaps. The ESA process from $^4I_{9/2}$ to $^4F_{3/2}$ resulting in the depopulation of the $^4I_{9/2}$ energy level was reported before [39] and may explain the weaker increase of the 801 nm emission ($^4I_{9/2} \rightarrow {}^4I_{15/2}$) at higher P (Fig. 4(c)). All these ET and ESA processes (bars: green 3, green 3a, green 4 and grey $\underline{4}$) become more pronounced with increasing P, which is reflected by the increasing depopulation of lower lying Er^{3+} energy levels (group 1, Fig. 4(b)) revealing therefore decreasing emission intensities. This simultaneously increases the population of higher Er^{3+} energy levels and favors the emissions of photons from these states (group 3, Fig. 4(d)) [39, 40].

The 427 nm luminescence assigned to the $^4G_{7/2} \rightarrow {}^4I_{11/2}$ transition shows the strongest increase in intensity with increasing P. To populate the $^4G_{7/2}$ energy level, the absorption of 4 or more photons via ET and ESA (grey bar, $\underline{4}$) processes is needed. According to Wegh et al., the emission at about 433 nm [28] can also arise from the energy level $^2F(2)_{7/2}$ (54.7×10^3 cm^{-1}) accompanied by additional emission bands at about 466 and 505 nm matching the previously mentioned 468 nm ($^2G_{7/2} \rightarrow {}^4I_{13/2}$), & ($^2P_{3/2} \rightarrow {}^4I_{11/2}$) and 503 nm ($^4G_{11/2} \rightarrow {}^4I_{13/2}$) luminescence bands. The Meijerink group [28] experimentally identified the $^4D_{1/2}$ emissive state (47.2×10^3 cm^{-1}) as origin for the emission bands located at about 378, 405, and 481 nm that are included in the energy schema shown in Fig. S6(g) in the ESM. For the population of the high energy states $^2F(2)_{7/2}$ and $^4D_{1/2}$ that requires theoretically the absorption of 7 or 8 photons we suggest an Er^{3+} to Er^{3+} ET ($Er^{3+} \rightarrow Er^{3+}$-ET) mechanism whereby one ET process occurs from a higher to a lower Er^{3+} energy level while the other ET process involves the transition from a lower to a higher Er^{3+} energy state. Such a coupled $Er^{3+} \rightarrow Er^{3+}$-ET could overcome the large energy gap rendering the energies of the 378 and 410 nm emission bands sufficient to populate the $^2F(2)_{7/2}$ state, as shown in Fig. S6(g) in the ESM. The energy differences between the transitions leading to the emission bands at 521, 541, 556, 616, 654, and 699 nm are apparently sufficient to populate the $^4D_{1/2}$ state via the proposed $Er^{3+} \rightarrow Er^{3+}$-ET process. This could also explain the decrease in intensity of the first group of emission bands (Fig. 4(b)) at a P of about 0.6 MW/cm^2 accompanied by a simultaneous increase of the intensities of the third group of emission bands (Fig. 4(d)).

In addition, also temperature effects at higher P can contribute to these observations, making some transitions with an energy mismatch more likely and favoring the population of higher energy levels responsible for the emission bands described in Figs. 4(c) and 4(d). Thermal effects caused by the high P of the focused laser beam used for sample excitation can be considered with the aid of the intensity ratios of the coupled $^4S_{3/2}$ (541 nm) and $^2H_{11/2}$ (521 nm) green emissive Er^{3+} levels presented in Fig. S6(i) in the ESM which are in a Boltzmann equilibrium and have been used before for temperature sensing [41]. With increasing P, an increased depopulation of the subjacent $^4S_{3/2}$ level to the higher $^2H_{11/2}$ level occurs for all 4 UCNP systems.

A comparison of the P-dependent UCL emission bands of all four UCNP systems (Fig. S6(h) in the ESM) reveals the same trends for the three groups of UCL emission bands and their dependencies on the Er^{3+} doping concentration.

2.4 Comparison of emission band ratios

Subsequently, we examined the P-dependence of the green-to-green (G/G) and green-to-red (G/R) intensity ratios to highlight the impact of doping and surface protection for the different P regimes (Fig. 5). In the G/R ratio the influence of the BET is included in contrast to the G/G ratio.

For the G/G ratios, we used the peak values of the 541 nm ($^4S_{3/2} \rightarrow {}^4I_{15/2}$) and the 556 nm ($^2H_{9/2} \rightarrow {}^4I_{13/2}$) emission bands in Fig. 5(a). For the lower P regime covered by the ensemble measurements of dispersed UCNPs, different G/G-peak ratios are observed for the co (black, red) and cs (blue, orange) UCNPs, independent of Er^{3+} doping concentration, thereby underlining the importance of UCNP surface protection. With increasing P, the differences in the G/G values of the core and core–shell UCNPs start to decrease due to the enhanced population rates of the Yb^{3+} and Er^{3+} energy levels compensating for quenching effects. At high P (> 0.1 MW/cm^2) applied in the SP studies, the G/G-peak ratios eventually converge to values of 0.4 and 0.65 for the samples doped with 1% and 3% Er^{3+}, respectively, almost independent of UCNP architecture. Similar results are obtained for the 541 to 654 nm ($^4F_{9/2} \rightarrow {}^4I_{15/2}$) peak ratios over the whole P range covered as illustrated in Fig. 5(b). The differences of the G/G and G/R ratios observed for higher P indicate the influence of the BET on the red emission. The G/R ratios presented on a logarithmic scale show a saddle point (1–10 kW/cm²) followed by decreasing ratios with local minima at about 0.6 MW/cm² and an increase for higher P. This behavior is attributed to the influence of BET and Yb^{3+} saturation as discussed in the previous section.

2.5 Luminescence decay kinetics

To provide a deeper insight into the (de)population processes responsible for UCL and the influence of ET and quenching processes for specific emissive energy levels, the Yb^{3+} and Er^{3+} UCL decay kinetics were investigated. The decay behavior of the green and red emission bands and the corresponding decay curves (together with the calculated intensity weighted lifetimes (LTs)) are shown in Fig. 6. Protecting UCNP cores with a 5 nm thick inert $NaYF_4$ shell significantly increases the lifetimes of the green and red UCL of both 1% and 3% Er^{3+} doped UCNPs under 980 nm Yb^{3+} excitation as to be expected from the diminished quenching of surface and near-surface

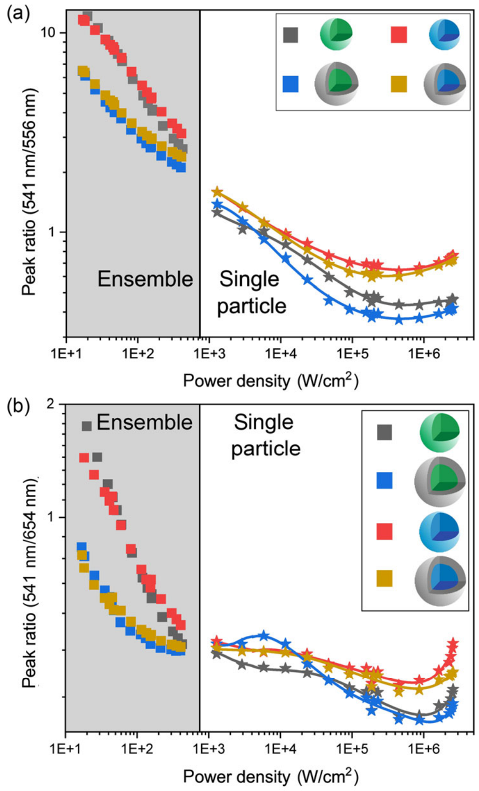

Figure 5 Double logarithmic plot of the *P*-dependent peak emission ratios of the four co and cs systems derived from measurements of UCNP ensembles dispersed in cyclohexane and single UCNPs dried on a glass substrate. (a) *P*-dependent green-to-green ratios (G/G) of the 541 and 556 nm peaks decreasing with increasing *P* and converge for $P > 0.1$ MW/cm^2 as illustrated by the solid curves that present only a guide to the eye. (b) *P*-dependent green-to-red ratios (G/R) of the 541 and 654 nm peaks revealing the decreasing trend for ensemble measurements and the behavior observed in the SP studies. The lines, that present only a guide to the eye show a plateau followed by a minimum at about 0.6 MW/cm², reflecting the influence of BET on the red emission.

Yb^{3+} ions. The small increase in activator concentration from 1% to 3% Er^{3+} leads to slightly faster decay kinetics and shorter LTs of the green and red Er^{3+} emission as derived from ensemble and single UCNP studies in Figs. 6(a) and 6(d). This is ascribed to a slightly accelerated energy migration between neighboring Er^{3+} ions and an increased probability for Er^{3+}–Er^{3+} CR processes [42]. For the small variation in Er^{3+} doping concentration employed in this study, these effects are, however, expectedly only moderate. To assess the influence of the different UCNP environments used for the ensemble and SP studies, we exemplarily performed time-resolved luminescence studies with single particles doped with 3% Er^{3+} first dried on glass and subsequently re-dispersed in cyclohexane (orange). The very small differences in the LTs of the green and red emission (see Figs. 6(a) and 6(d)) underline the negligible influence of cyclohexane on the UCL decay kinetics at high *P*.

2.5.1 *Comparing decay kinetics of ensemble and single particle studies*

For the green Er^{3+} emission, the core UCNPs show shorter LTs in the ensemble than in the SP studies while for core–shell UCNPs, the opposite trend is observed as shown in Figs. 6(a) and 6(d). A direct comparison of the results of ensemble and single particle studies is challenging for nonlinear emitters like UCNPs due to the strong difference in *P* used for both types of measurements. Moreover, as discussed previously, a spectral overlap of some emission bands occurring for high *P* can also affect the resulting decay kinetics. This is particularly challenging in the green wavelength region as for single UCNP studies a bandpass filter covering the wavelength region from 533–557 nm (see Fig. 6(c)) was used. For the red emission the bandpass filter covering the spectral window of 635–675 nm was employed (see Fig. 6(f)). Thereby, a contribution from the 639 nm emission band ($^2K_{15/2} \rightarrow {}^4I_{9/2}$) cannot be discriminated from the red Er^{3+} emission centered at about 655 nm. The pronounced contribution of the emission band at 556 nm ($^2H_{9/2} \rightarrow {}^4I_{13/2}$, Fig. 4(e)) originating from higher lying Er^{3+} energy levels, that cannot be spectrally

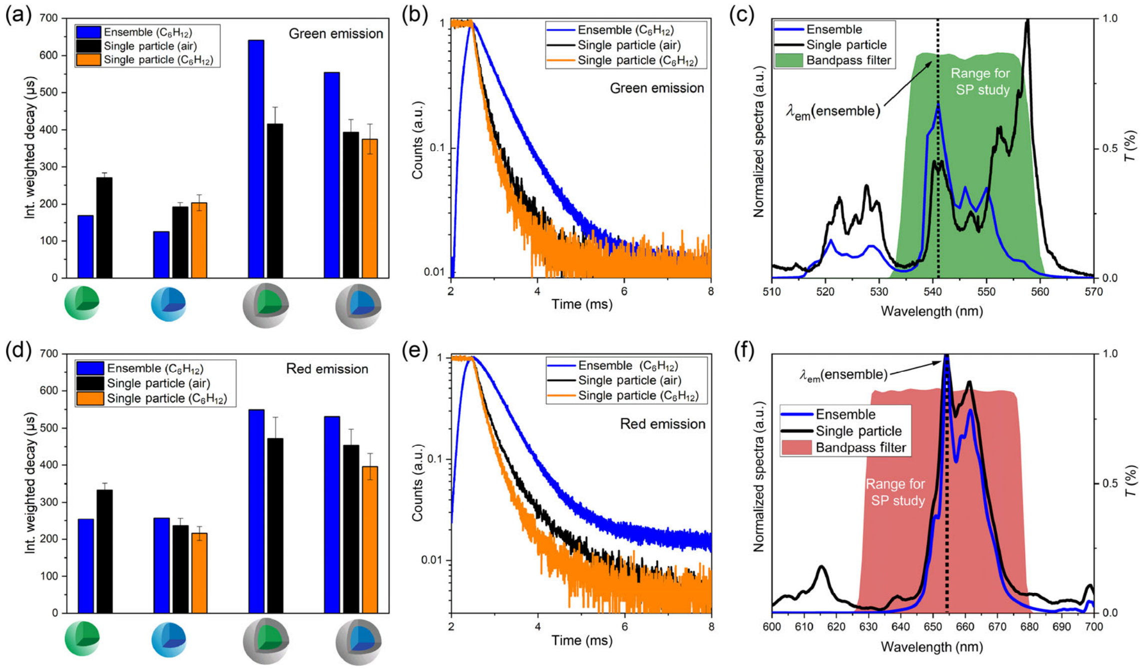

Figure 6 Luminescence decay kinetics of the four core-only and core–shell UCNP systems. (a) and (d) Intensity weighted lifetimes of the green (a) and red (d) emission obtained from ensemble measurements of UCNPs dispersed in cyclohexane (blue) and derived from SP studies of dried UCNPs in air (black) and UCNPs re-dispersed in cyclohexane (orange; for UCNPs doped with 3% Er^{3+}). (b) and (e) Decay curves of the green and red emission determined for the core–shell UCNPs containing 3% Er^{3+} using different measurement conditions. (c) and (f) Comparison of the wavelength regions used for the ensemble and SP studies employing a monochromator and bandpass filters for spectral separation of the green and red emission.

separated from 541 nm emission, contributes to the determined LTs with faster intrinsic decay rates. The LT of 19.5 µs obtained for the $^2H_{9/2}$ level [16] is most likely responsible for the shorter LTs of single cs UCNPs compared to ensemble measurements. This suggests that contributions from higher energy transitions excited at high *P* result in effectively accelerated luminescence decay kinetics. The decay behavior of the red emission shows the same trends as the green UCL except for the core UCNPs doped with 3% Er^{3+}, for which slightly longer LTs are obtained in the ensemble studies.

The comparably small influence of the excitation pulse width for SP measurements is discussed in Fig. S8 in the ESM.

3 Conclusion and outlook

In summary, we performed excitation *P*-dependent UCL studies of core and core–shell β-$NaYF_4$:Yb,Er UCNPs doped with 20% Yb^{3+} and 1% or 3% Er^{3+} varying *P* over 6 orders of magnitude to gain deeper mechanistic insights into (de)population processes at high *P*. Therefore, to expand the *P* regime covered by our integrating sphere setup used for UCNP ensemble measurements (5 to 400 W/cm^2) we built up a new widefield and confocal laser scanning microscopy setup allowing measurements in a *P* range of 1 kW/cm^2 to 2.6 MW/cm^2 with SPs. The several newly observed Er^{3+} emission bands in the UV/vis/NIR at high *P* that changed the overall emission color of the UCNPs from green over yellow to eventually white were categorized into three groups depending on the number of photons involved in the underlying UC processes, i.e., 2–3, 3–4 or 4 photons and their different *P*-dependencies. The first group of Er^{3+} emissions showed maximum emission intensities at *P* of about 600 kW/cm^2. The second group became visible at $P > 10$ kW/cm^2 and started to saturate for $P > 0.6$ MW/cm^2. The emission bands of the third group appeared at $P > 100$ kW/cm^2 and grew at the expense of the bands of the first group. These emission bands resulted from higher energy Er^{3+} states populated from very high-energy levels of Er^{3+} with minor contributions from laser induced heating effects.

By exploiting the green-to-green (541 nm/556 nm) and the green-to-red (541 nm/654 nm) peak ratios we combined the results of the ensemble and SP studies of these UCNPs. This indicates that the parameters controlling the UCL behavior at low and medium *P* are the thickness and tightness of the surface-protecting shell and at high *P* the concentration of the lanthanide doping ions, which becomes already apparent even for the only slightly varied Er^{3+} doping concentrations of 1% and 3%. Higher Yb^{3+} and Er^{3+} doping ratios are expected to further enhance UCNP brightness in microscopy studies at high *P* as recently suggested [21, 43–45]. For luminescence decay studies the additional contributions from higher transitions at high *P* can result in effectively accelerated decay kinetics for the SP studies.

In addition, our results underline the importance to correctly determine and report the *P* values used for the evaluation of UCL spectra and UCL decay kinetics. Moreover, our UCL spectra obtained at high *P* clearly illustrate the need to clarify a possible spectral overlap of closely lying emission bands and to consider such effects also for UCL lifetime measurements in SP studies. This—in conjunction with the need for spectrally corrected emission spectra, that take the wavelength-dependent spectral responsivity of the detection system into account—must be considered to improve the general comparability of UCL data obtained by different research groups with different setups.

In the future, we plan to systematically prepare and study UCNP systems varying strongly in Yb^{3+} and Er^{3+} doping concentration on the ensemble and SP level, thereby aiming to provide a quantitative experimental basis for developing brighter UCNPs for different application-relevant *P* regimes with precise color control and color tuning.

4 Experimental

4.1 Chemicals

Lanthanide chloride hexahydrates (> 99.9%) were obtained from Sigma Aldrich and Treibacher Industrie AG. Oleic acid and 1-octadecene (both technical grade, 90%) were purchased from Alfa Aesar. Ammonium fluoride and sodium hydroxide, both of analytical grade, were purchased from Sigma Aldrich. All other chemicals were of analytical grade and were obtained from Sigma Aldrich, Merck or Acros. All chemicals were used as received without further purification.

4.2 Synthesis

The synthesis of core UCNPs started from rare earth trichlorides (1 mmol), using the doping ratios desired for UCNP doping, dissolved in methanol, which were heated up to 160 °C under nitrogen atmosphere, in a mixture of 1-octadecene (15 mL) and oleic acid (6 mL). Vacuum was applied for 30 min to yield a clear solution. The solution was cooled to room temperature and 0.148 g (4.0 mmol) NH_4F and 0.1 g (2.5 mmol) NaOH dissolved in methanol were added. The suspension was kept at 120 °C for 30 min, heated to reflux (approx. 325 °C), and kept at this temperature for approx. 10 min before the reaction was stopped and the mixture was cooled to room temperature. The particles were precipitated by addition of excess ethanol and collected by centrifugation at 1,000 g for 5 min. The precipitate was washed twice with chloroform/ethanol and 3 times with cyclohexane/acetone by repeated re-dispersion precipitation centrifugation cycles.

The shell precursor material ($NaYF_4$) was prepared identically until the heating step to reflux. Here, the reaction mixture was heated to 240 °C for 40 min before it was cooled down to room temperature. The purification process was the same as described above. Core–shell particles were synthesized by seed-mediated shell growth. The shell precursor material and the core particles were each suspended in a mixture of 5 mL oleic acid and 5 mL 1-octadecene per 1 mmol $NaYF_4$. The precursors were kept at 120 °C under N_2 flow while the core particles were heated to reflux (325 °C) under N_2 flow. Small volumes (3 mL at most) of the hot precursor mixture were injected into the boiling reaction mixture every 10 min. The mixture was cooled down to room temperature 10 min after the last injection. The purification process was the same as described above.

4.3 Particle characterisation

Inductively coupled plasma (ICP), transmission electron microscopy (TEM), X-ray diffraction (XRD) and dynamic light scattering (DLS) results are shown in Sections S1 and S2 in the ESM.

4.4 Ensemble studies

The *P*-dependent UCL spectra and upconversion quantum yields (ϕ_{UC}) of the UCNP dispersions were measured at 978 nm excitation employing a custom-made integrating sphere setup equipped with an 8 W laser diode and density filter sets covering power densities from 5 to 400 W/cm^2 [16]. The UCL decay kinetics were measured on dispersed NPs at an excitation wavelength of 980 nm using the fluorescence spectrometer FLS980 from Edinburgh Instruments. The *P* of the laser pulses

(400 µs pulse width) was measured averaged per pulse width at the focal plane as 63 W/cm^2. The lifetimes of the green and red UCL of Er^{3+} were obtained from bi-exponential tail-fits of the decay curves with the software Fluorescence Analysis Software Technology (FAST) from Edinburgh Instruments.

4.5 Single NP studies

Widefield (WF) luminescence imaging of UCNPs was performed with an inverted fluorescence microscope. The sample preparation and the setup are detailed in Section S3 in the ESM.

For *P*-dependent measurements of luminescence spectra and decay kinetics, a confocal microscope setup was used (Section S4 in the ESM). UCNPs were deposited via drop casting onto a glass substrate and AFM measurements were used to identify isolated single UCNPs for subsequent optical characterization. The light of a 976 nm continuous wave (cw) or pulsed laser diode (LDH-D-F-980, PicoQuant, Germany; pulsed with varying repetition rates of 0.25 to 80 MHz) was focused onto the sample through a 100× oil-immersion objective with a numerical aperture of 1.4 (UPLSAPO100XO/1.4, Olympus). For the detection of the luminescence decay kinetics, the emitted light was separated from the excitation light with a dichroic mirror (F73-877SG, AHF, Germany) collected with two avalanche photodiodes (APD) (PDM series, PicoQuant, Germany) after separation by a 50/50 Pellicle-beam-splitter. A green (545 ± 12.5 nm; F49-546) and a red (655 ± 20 nm; F39-655) filter (AHF Analysetechnik AG, Germany) were placed in front of the APDs for the simultaneous detection of the green and red UCL. The APD signals and the synchronization signal of the laser (laser sync) were read out with a time correlated single photon counting (TCSPC) module (TimeHarp 260 PICO Dual, PicoQuant, Germany). The decay kinetics were measured under 980 nm excitation on dried UCNPs at high *P* (230 W/cm^2; 1 ms pulse width) for all four NP systems and exemplarily on 3% Er^{3+} after re-dispersion in cyclohexane. The decays were fitted with the SymPhoTime 64 software from PicoQuant. The *P*-dependent spectra were recorded with a CCD camera iDus420 from ANDOR. Therefore, the laser intensity was varied regarding output power (30% to 100%) in the cw mode and by continuously pulsed repetition with rates between 0.25 and 80 MHz, covering a *P* range of 1×10^3 to 2.6×10^6 W/cm^2.

Acknowledgements

The authors thank the European Upconversion Network (EUN) for financial support of a research exchange program (COST-CM1403). U. R.-G., F. F. and C. W. acknowledge financial support by research grants RE 1203/20-1 (project NANOHYPE; DFG and M-Eranet). Y. M. is grateful to the Institut Universitaire de France (IUF) for support and providing additional time to be dedicated to research.

Funding note: Open Access funding enabled and organized by Projekt DEAL.

Electronic Supplementary Material: Supplementary material (nanoparticle characterizations including ICP, TEM, XRD and DLS data; measurement conditions and setup used for widefield imaging; setup description of CLSM used for *P*-dependent SP studies; AFM scans; *P*-dependent spectra of all four NP systems; detailed Dieke diagram for Yb-Er transitions including high power excitation via Er→Er-ET processes; *P*-dependent band emission trends and CIE diagram of all four NP systems; green-to-green emission ratio; total-to-red area emission ratio; *P*-dependent green and red decay behavior) is available in the online version of this article at https://doi.org/10.1007/s12274-021-3350-y.

References

[1] Auzel, F. Upconversion and anti-stokes processes with f and d ions in solids. *Chem. Rev.* **2004**, *104*, 139–174.

[2] Wu, X.; Chen, G. Y.; Shen, J.; Li, Z. J.; Zhang, Y. W.; Han, G. Upconversion nanoparticles: A versatile solution to multiscale biological imaging. *Bioconjugate Chem.* **2015**, *26*, 166–175.

[3] Xu, C. T.; Zhan, Q. Q.; Liu, H. C.; Somesfalean, G.; Qian, J.; He, S. L.; Andersson-Engels, S. Upconverting nanoparticles for pre-clinical diffuse optical imaging, microscopy and sensing: Current trends and future challenges. *Laser Photonics Rev.* **2013**, *7*, 663–697.

[4] Wang, H. Q.; Batentschuk, M.; Osvet, A.; Pinna, L.; Brabec, C. J. Rare-earth ion doped up-conversion materials for photovoltaic applications. *Adv. Mater.* **2011**, *23*, 2675–2680.

[5] Gnach, A.; Bednarkiewicz, A. Lanthanide-doped up-converting nanoparticles: Merits and challenges. *Nano Today* **2012**, *7*, 532–563.

[6] Wang, F.; Liu, X. G. Recent advances in the chemistry of lanthanide-doped upconversion nanocrystals. *Chem. Soc. Rev.* **2009**, *38*, 976–989.

[7] Xu, J. T.; Gulzar, A.; Yang, P. P.; Bi, H. T.; Yang, D.; Gai, S. L.; He, F.; Lin, J.; Xing, B. G.; Jin, D. Y. Recent advances in near-infrared emitting lanthanide-doped nanoconstructs: Mechanism, design and application for bioimaging. *Coord. Chem. Rev.* **2019**, *381*, 104–134.

[8] Wu, X.; Zhang, Y. W.; Takle, K.; Bilsel, O.; Li, Z. J.; Lee, H.; Zhang, Z. J.; Li, D. S.; Fan, W.; Duan, C. Y. et al. Dye-sensitized core/active shell upconversion nanoparticles for optogenetics and bioimaging applications. *ACS Nano* **2016**, *10*, 1060–1066.

[9] Hososhima, S.; Yuasa, H.; Ishizuka, T.; Hoque, M. R.; Yamashita, T.; Yamanaka, A.; Sugano, E.; Tomita, H.; Yawo, H. Near-infrared (NIR) up-conversion optogenetics. *Sci. Rep.* **2015**, *5*, 16533.

[10] Pliss, A.; Ohulchanskyy, T. Y.; Chen, G. Y.; Damasco, J.; Bass, C. E.; Prasad, P. N. Subcellular optogenetics enacted by targeted nanotransformers of near-infrared light. *ACS Photonics* **2017**, *4*, 806–814.

[11] Chen, S.; Weitemier, A. Z.; Zeng, X.; He, L. M.; Wang, X. Y.; Tao, Y. Q.; Huang, A. J. Y.; Hashimotodani, Y.; Kano, M.; Iwasaki, H. et al. Near-infrared deep brain stimulation via upconversion nanoparticle-mediated optogenetics. *Science* **2018**, *359*, 679–684.

[12] Lu, Y. Q.; Zhao, J. B.; Zhang, R.; Liu, Y. J.; Liu, D. M.; Goldys, E. M.; Yang, X. S.; Xi, P.; Sunna, A.; Lu, J. et al. Tunable lifetime multiplexing using luminescent nanocrystals. *Nat. Photonics* **2014**, *8*, 32–36.

[13] Goldschmidt, J. C.; Fischer, S. Upconversion for photovoltaics—A review of materials, devices and concepts for performance enhancement. *Adv. Opt. Mater.* **2015**, *3*, 510–535.

[14] Liu, Y. J.; Lu, Y. Q.; Yang, X. S.; Zheng, X. L.; Wen, S. H.; Wang, F.; Vidal, X.; Zhao, J. B.; Liu, D. M.; Zhou, Z. G. et al. Amplified stimulated emission in upconversion nanoparticles for super-resolution nanoscopy. *Nature* **2017**, *543*, 229–233.

[15] Kraft, M.; Würth, C.; Muhr, V.; Hirsch, T.; Resch-Genger, U. Particle-size-dependent upconversion luminescence of $NaYF_4$: Yb, Er nanoparticles in organic solvents and water at different excitation power densities. *Nano Res.* **2018**, *11*, 6360–6374.

[16] Kaiser, M.; Würth, C.; Kraft, M.; Hyppänen, I.; Soukka, T.; Resch-Genger, U. Power-dependent upconversion quantum yield of $NaYF_4$: Yb^{3+}, Er^{3+} nano-and micrometer-sized particles–measurements and simulations. *Nanoscale* **2017**, *9*, 10051–10058.

[17] Würth, C.; Kaiser, M.; Wilhelm, S.; Grauel, B.; Hirsch, T.; Resch-Genger, U. Excitation power dependent population pathways and absolute quantum yields of upconversion nanoparticles in different solvents. *Nanoscale* **2017**, *9*, 4283–4294.

[18] Wilhelm, S.; Kaiser, M.; Wurth, C.; Heiland, J.; Carrillo-Carrion, C.; Muhr, V.; Wolfbeis, O. S.; Parak, W. J.; Resch-Genger, U.; Hirsch, T. Water dispersible upconverting nanoparticles: Effects of surface modification on their luminescence and colloidal stability. *Nanoscale* **2015**, *7*, 1403–1410.

[19] Wiesholler, L. M.; Hirsch, T. Strategies for the design of bright upconversion nanoparticles for bioanalytical applications. *Opt. Mater.* **2018**, *80*, 253–264.

[20] Ohulchanskyy, T. Y.; Roy, I.; Yong, K. T.; Pudavar, H. E.; Prasad, P. N. High-resolution light microscopy using luminescent nanoparticles. *Wiley Interdiscip. Rev. Nanomed. Nanobiotechnol.* **2010**, *2*, 162–175.

[21] Gargas, D. J.; Chan, E. M.; Ostrowski, A. D.; Aloni, S.; Altoe, M. V. P.; Barnard, E. S.; Sanii, B.; Urban, J. J.; Milliron, D. J.; Cohen, B. E. et al. Engineering bright sub-10-nm upconverting nanocrystals for single-molecule imaging. *Nat. Nanotechnol.* **2014**, *9*, 300–305.

[22] Zhou, J. J.; Xu, S. Q.; Zhang, J. J.; Qiu, J. R. Upconversion luminescence behavior of single nanoparticles. *Nanoscale* **2015**, *7*, 15026–15036.

[23] Liu, Q.; Zhang, Y. X.; Peng, C. S.; Yang, T. S.; Joubert, L. M.; Chu, S. Single upconversion nanoparticle imaging at sub-10 W cm^{-2} irradiance. *Nat. Photonics* **2018**, *12*, 548–553.

[24] Yuan, M.; Wang, R.; Zhang, C.; Yang, Z.; Cui, W.; Yang, X.; Xiao, N.; Wang, H.; Xu, X. Exploiting the silent upconversion emissions from a single β-$NaYF_4$: Yb/Er microcrystal via saturated excitation. *J. Mater. Chem. C* **2018**, *6*, 10226–10232.

[25] Muhr, V.; Würth, C.; Kraft, M.; Buchner, M.; Baeumner, A. J.; Resch-Genger, U.; Hirsch, T. Particle-size-dependent forster resonance energy transfer from upconversion nanoparticles to organic dyes. *Anal. Chem.* **2017**, *89*, 4868–4874.

[26] Dukhno, O.; Przybilla, F.; Muhr, V.; Buchner, M.; Hirsch, T.; Mély, Y. Time-dependent luminescence loss for individual upconversion nanoparticles upon dilution in aqueous solution. *Nanoscale* **2018**, *10*, 15904–15910.

[27] Sardar, D. K.; Gruber, J. B.; Zandi, B.; Hutchinson, J. A.; Trussell, C. W. Judd–Ofelt analysis of the $Er^{3+}(4f^{11})$ absorption intensities in phosphate glass: Er^{3+}, Yb^{3+}. *J. Appl. Phys.* **2003**, *93*, 2041–2046.

[28] Wegh, R. T.; Van Loef, E. V. D.; Burdick, G. W.; Meijerink, A. Luminescence spectroscopy of high-energy $4f^{11}$ levels of Er^{3+} in fluorides. *Mol. Phys.* **2003**, *101*, 1047–1056.

[29] O'Shea, D. G.; Ward, J. M.; Shortt, B. J.; Mortier, M.; Féron, P.; Chormaic, S. N. Upconversion channels in Er^{3+}: ZBLALiP fluoride glass microspheres. *Eur. Phys. J. Appl. Phys.* **2007**, *40*, 181–188.

[30] Chen, X. Y.; Ma, E.; Liu, G. K. Energy levels and optical spectroscopy of Er^{3+} in Gd_2O_3 nanocrystals. *J. Phys. Chem. C* **2007**, *111*, 10404–10411.

[31] Cheng, Z. X.; Zhang, S. J.; Song, F.; Guo, H. C.; Han, J. R.; Chen, H. C. Optical spectroscopy of Yb/Er codoped $NaY(WO_4)_2$ crystal. *J. Phys. Chem. Solids* **2002**, *63*, 2011–2017.

[32] Marciniak, L.; Waszniewska, K.; Bednarkiewicz, A.; Hreniak, D.; Strek, W. Sensitivity of a nanocrystalline luminescent thermometer in high and low excitation density regimes. *J. Phys. Chem. C* **2016**, *120*, 8877–8882.

[33] Lei, Y. Q.; Song, H. W.; Yang, L. M.; Yu, L. X.; Liu, Z. X.; Pan, G. H.; Bai, X.; Fan, L. B. Upconversion luminescence, intensity saturation effect, and thermal effect in Gd_2O_3: Er^3, Yb^{3+} nanowires. *J. Chem. Phys.* **2005**, *123*, 174710.

[34] Bhiri, N. M.; Dammak, M.; Aguiló, M.; Díaz, F.; Carvajal, J. J.; Pujol, M. C. Stokes and anti-Stokes operating conditions dependent luminescence thermometric performance of Er^{3+}-doped and Er^{3+}, Yb^{3+} co-doped $GdVO_4$ microparticles in the non-saturation regime. *J. Alloys Compd.* **2020**, *814*, 152197.

[35] Berry, M. T.; May, P. S. Disputed mechanism for nir-to-red upconversion luminescence in $NaYF_4$: Yb^{3+}, Er^{3+}. *J. Phys. Chem. A* **2015**, *119*, 9805–9811.

[36] Cho, Y.; Song, S. W.; Lim, S. Y.; Kim, J. H.; Park, C. R.; Kim, H. M. Spectral evidence for multi-pathway contribution to the upconversion pathway in $NaYF_4$: Yb^{3+}, Er^{3+} phosphors. *Phys. Chem. Chem. Phys.* **2017**, *19*, 7326–7332.

[37] Kaiser, M.; Würth, C.; Kraft, M.; Soukka, T.; Resch-Genger, U. Explaining the influence of dopant concentration and excitation power density on the luminescence and brightness of β-$NaYF_4$: Yb^{3+}, Er^{3+} nanoparticles: Measurements and simulations. *Nano Res.* **2019**, *12*, 1871–1879.

[38] Rabouw, F. T.; Prins, P. T.; Villanueva-Delgado, P.; Castelijns, M.; Geitenbeek, R. G.; Meijerink, A. Quenching pathways in $NaYF_4$: Er^{3+}, Yb^{3+} upconversion nanocrystals. *ACS Nano* **2018**, *12*, 4812–4823.

[39] Lyapin, A. A.; Gushchin, S. V.; Ermakov, A. S.; Kuznetsov, S. V.; Ryabochkina, P. A.; Proydakova, V. Y.; Voronov, V. V.; Fedorov, P. P.; Chernov, M. V. Mechanisms and absolute quantum yield of upconversion luminescence of fluoride phosphors. *Chin. Opt. Lett.* **2018**, *16*, 091901.

[40] Golesorkhi, B.; Fürstenberg, A.; Nozary, H.; Piguet, C. Deciphering and quantifying linear light upconversion in molecular erbium complexes. *Chem. Sci.* **2019**, *10*, 6876–6885.

[41] Vetrone, F.; Naccache, R.; Zamarrón, A.; De La Fuente, A. J.; Sanz-Rodríguez, F.; Maestro, L. M.; Rodriguez, E. M.; Jaque, D.; Solé, J. G.; Capobianco, J. A. Temperature sensing using fluorescent nanothermometers. *ACS Nano* **2010**, *4*, 3254–3258.

[42] Bergstrand, J.; Liu, Q. Y.; Huang, B. R.; Peng, X. Y.; Würth, C.; Resch-Genger, U.; Zhan, Q. Q.; Widengren, J.; Ågren, H.; Liu, H. C. On the decay time of upconversion luminescence. *Nanoscale* **2019**, *11*, 4959–4969.

[43] Wang, Z. J.; Meijerink, A. Concentration quenching in upconversion nanocrystals. *J. Phys. Chem. C* **2018**, *122*, 26298–26306.

[44] Tan, M. L.; Monks, M. J.; Huang, D. X.; Meng, Y. J.; Chen, X. W.; Zhou, Y.; Lim, S. F.; Würth, C.; Resch-Genger, U.; Chen, G. Y. Efficient sub-15 nm cubic-phase core/shell upconversion nanoparticles as reporters for ensemble and single particle studies. *Nanoscale* **2020**, *12*, 10592–10599.

[45] Chen, B.; Wang, F. Combating concentration quenching in upconversion nanoparticles. *Acc. Chem. Res.* **2020**, *53*, 358–367.